Solar Phys (2009) 259: 227–254
DOI 10.1007/s11207-009-9382-1

Relation Between Type II Bursts and CMEs Inferred from STEREO Observations

N. Gopalswamy · W.T. Thompson · J.M. Davila · M.L. Kaiser · S. Yashiro · P. Mäkelä · G. Michalek · J.-L. Bougeret · R.A. Howard

Received: 24 December 2008 / Accepted: 21 May 2009 / Published online: 20 June 2009

Abstract The inner coronagraph (COR1) of the *Solar Terrestrial Relations Observatory* (STEREO) mission has made it possible to observe CMEs in the spatial domain overlapping with that of the metric type II radio bursts. The type II bursts were associated with generally weak flares (mostly B and C class soft X-ray flares), but the CMEs were quite energetic. Using CME data for a set of type II bursts during the declining phase of solar cycle 23, we determine the CME height when the type II bursts start, thus giving an estimate of the heliocentric distance at which CME-driven shocks form. This distance has been determined to be $\sim 1.5 R_s$ (solar radii), which coincides with the distance at which the Alfvén speed profile has a minimum value. We also use type II radio observations from STEREO/WAVES and *Wind*/WAVES observations to show that CMEs with moderate speed drive either weak shocks or no shock at all when they attain a height where the Alfvén speed peaks ($\sim 3 R_s$ – $4 R_s$). Thus the shocks seem to be most efficient in accelerating electrons in the heliocentric distance range of $1.5 R_s$ to $4 R_s$. By combining the radial variation of the CME speed in the inner corona (CME speed increase) and interplanetary medium (speed decrease) we were able to correctly account for the deviations from the universal drift-rate spectrum of type II bursts, thus confirming the close physical connection between type II bursts and CMEs. The

STEREO Science Results at Solar Minimum
Guest Editors: Eric R. Christian, Michael L. Kaiser, Therese A. Kucera, O.C. St. Cyr

N. Gopalswamy (✉) · W.T. Thompson · J.M. Davila · M.L. Kaiser
NASA Goddard Space Flight Center, Greenbelt, MD, USA
e-mail: nat.gopalswamy@nasa.gov

S. Yashiro
Interferometrics, Herndon, VA, USA

P. Mäkelä · G. Michalek
The Catholic University of America, Washington, DC, USA

J.-L. Bougeret
Paris Observatory, Meudon, France

R.A. Howard
Naval Research Laboratory, Washington, DC, USA

average height ($\sim 1.5 R_s$) of STEREO CMEs at the time of type II bursts is smaller than that ($2.2 R_s$) obtained for SOHO (*Solar and Heliospheric Observatory*) CMEs. We suggest that this may indicate, at least partly, the density reduction in the corona between the maximum and declining phases, so a given plasma level occurs closer to the Sun in the latter phase. In two cases, there was a diffuse shock-like feature ahead of the main body of the CME, indicating a standoff distance of $1 R_s - 2 R_s$ by the time the CME left the LASCO field of view.

Keywords Coronal mass ejections · Type II radio bursts · Shocks · Flares · Dynamic spectrum

1. Introduction

One of the major disadvantages in studying the physical relation between coronal mass ejections (CMEs) and metric type II radio bursts has been the lack of spatial overlap between the observations. Since a type II burst is the earliest signature of a shock, identifying the CME leading edge at the time of the metric type II burst provides an estimate of the height at which the shock forms. Knowing the heliocentric distance at which the shock forms is important in understanding many aspects of CMEs such as the charge state composition of solar energetic particles observed in the interplanetary medium. Using the height – time plots of white-light CMEs observed by the Large Angle and Spectrometric Coronagraph (LASCO, Brueckner *et al.*, 1995) onboard the *Solar and Heliospheric Observatory* (SOHO) mission, Gopalswamy *et al.* (2005) found an average CME height of $\sim 2.2 R_s$ at the onset of metric type II bursts. This result was based on type II bursts originating from close to the limb (central meridian distance, CMD, between 60° and 90°), so the projection effects are minimal and hence the height measurements are accurate. Unfortunately, the SOHO/LASCO occulting disk obscured the corona to a heliocentric distance of $\sim 2.5 R_s$. This means that type II bursts typically start when the CMEs are still below the occulting disk. Therefore, the CME height – time plots from SOHO/LASCO have to be extrapolated to the times of type II bursts to estimate the CME heights. The expanded field of view (FOV) of the inner coronagraph (COR1) of the Sun Earth Connection Coronal and Heliospheric Investigation (SECCHI; Howard *et al.*, 2008) instrument onboard the *Solar TErrestrial RElations Observatory* (STEREO; Kaiser *et al.*, 2008) mission has changed this situation by providing CME height measurements down to $1.4 R_s$. This is an important new capability for type II burst studies because the COR1 FOV overlaps with the spatial domain of the corona where the type II bursts start (Gopalswamy and Kaiser, 2002). Furthermore, the outer coronagraph (COR2) on SECCHI overlaps with the LASCO FOV for consistency check. The present study makes use of the COR1 capability to determine CME heights at the onset of type II bursts without extrapolation.

A related problem is the evolution of the CME in the inner corona. Since the CME starts from rest as it erupts, it undergoes rapid acceleration in the beginning, reaching a maximum acceleration in the inner corona before being controlled by the aerodynamic drag (Wood *et al.*, 1999; Gopalswamy and Thompson, 2000; Zhang *et al.*, 2001; Vršnak, 2001). The CME acceleration occurs at a heliocentric distance where the characteristic speed in the corona attains a minimum in the periphery of active regions (Gopalswamy *et al.*, 2001a; Mann *et al.*, 2003) before reaching a peak in the outer corona (Mann *et al.*, 1999; Gopalswamy *et al.*, 2001a). Since the CME speed needs to exceed the characteristic speed before it can drive a shock, the combination of CME acceleration and the rapid change in the fast-mode

speed produces interesting possibilities for shock formation and decay (Gopalswamy *et al.*, 2001a). STEREO/COR1 provides CME measurements in this important spatial domain and hence can capture the early evolution of CMEs. In addition, SECCHI's Extreme Ultraviolet Imager (EUVI) obtains high-cadence images, providing information on the CME and the surrounding EUV waves very close to the solar surface.

Information on the early evolution of CMEs has important implications for understanding the spectral evolution of type II bursts throughout the inner heliosphere. It is well known that the frequency drift rate of type II bursts in the radio dynamic spectra are related to the speed of the shock that produces the bursts and the density gradient in the ambient medium. It was noted by several authors that the frequency drift rate is a power law in the frequency of emission (Mann *et al.*, 1996; Vršnak *et al.*, 2001, 2002; Aguilar-Rodriguez *et al.*, 2005). The power law was found to be valid when observations from different spectral domains [metric (m), decameter – hectometric (DH), and kilometric (km) wavelengths] are combined for the same events or for different events. Similarly, the power law was maintained when observations from different instruments and different epochs are combined. This universal nature of the power law suggests that the same shock should be involved in producing radio bursts at various spectral domains. In the spatial domain, this means the propagation of CME-driven shocks starting near the Sun and propagating far into the interplanetary medium (Gopalswamy, 2006b). One of the assumptions we make in this paper is that the heliocentric distance of the type II burst (and of the shock) can be approximated by that of the driving CME. We also assume that the shock speed is similar to the CME speeds. The shock is expected to surround the CME as a bow wave at the standoff distance. Near the Sun, the standoff distance may not be too large. However, the electrons responsible for the type II burst may be accelerated at the shock flanks (Holman and Pesses, 1983), which means the heliocentric distance of the type II burst location may be smaller than the CME leading edge. Thus, the CME height is a reasonable approximation to the heliocentric distance of the shock, especially because of the lack of spatial information for the type II burst. The analyses in this paper adheres to one of the paradigms of type II radio bursts that CME-driven shocks can explain type II bursts in all wavelength domains. We do appreciate that there is an alternative paradigm that flare blast waves produce some metric type II bursts (see Vršnak and Cliver, 2008, for a review on this topic). We shall show that the data and results presented in this paper are more consistent with the CME-driven shock paradigm.

We study all the metric type II radio bursts and their interplanetary counterparts observed since the launch of the STEREO mission, in conjunction with the CMEs and flares associated with the bursts. In Section 2, we describe the radio and optical data used in this paper and arrive at some overall conclusions about the type II bursts and the associated CMEs. In Section 3, we describe four type II bursts and the associated CMEs in detail and connect the CME speed evolution to the duration of the type II burst by addressing the parallel evolution of the Alfvén speed profile in the corona. In one event, the type II burst was observed in the interplanetary (IP) medium, which we connect to the CME evolution in the outer corona. In Section 4 we show that the deviations from the universal drift-rate spectrum of type II bursts can be explained by the opposite tendencies in the radial variation of CME speed in the metric and IP domains of type II radio bursts. Section 5 discusses the results and provides a summary.

2. Data Description and Overview

We collected information on type II radio bursts that occurred during January 2007 to November 2008 from two main sources: *i*) the list of metric type II radio bursts archived at the

Table 1 Spatial resolution and field of view of instruments from SOHO and STEREO used in this paper.

	Pixel Size	CCD Size	FOV	Cadence (minutes)
EIT 195	2.6″	1024 × 1024	0 − 1.4R_s	12
LASCO C2	11.2″	1024 × 1024	2.1 − 6.0R_s	∼ 20
LASCO C3	56.0″	1024 × 1024	3.7 − 30R_s	∼ 30
SECCHI EUVI	1.6″	2048 × 2048	0 − 1.7R_s	2.5
SECCHI COR1	3.75″	2048 × 2048	1.4 − 4R_s	5 or 10
	(7.5″)	(1024 × 1024)		
SECCHI COR2	14.7″	2048 × 2048	2 − 15R_s	15

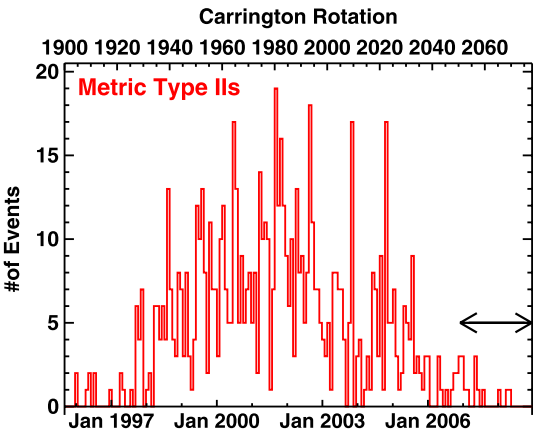

Figure 1 Occurrence rate of metric type II bursts binned over Carrington rotation periods from 1996 to November 2008. The study period is indicated by the double arrow. The Carrington rotation numbers are shown in the top. During solar maximum, the highest rate was 19 type II bursts per rotation.

National Geophysical Data Center (NGDC) and available online (ftp://ftp.ngdc.noaa.gov/STP/SOLAR_DATA/SOLAR_RADIO/SPECTRAL) and at the online *Solar Geophysical Data* (SGD) and *ii*) the list of type II bursts in the DH and km wavelengths detected by the Radio and Plasma Wave Experiments onboard *Wind* and STEREO (Bougeret *et al.*, 1995, 2008) available at http://lep694.gsfc.nasa.gov/waves/waves.html. We also compared the two lists to see whether any of the metric type II bursts had DH counterparts and *vice versa*. For each type II burst, we identified the associated CME from STEREO and SOHO instruments that image the corona in EUV and/or white light. The COR1 FOV extends from 1.4R_s to 4R_s but, when combined with the SECCHI/EUVI and the Extreme-ultraviolet Imaging Telescope (EIT) onboard SOHO, we can observe the CMEs all the way to the surface. The combined data set thus provides an opportunity to track CMEs and the associated disturbances up to a heliocentric distance of 32R_s from close to the solar surface. The SECCHI heliospheric imagers extend the FOV all the way to Earth orbit, but we do not use the data in this study because most of the type II bursts were confined to frequencies that correspond to the near-Sun part of the interplanetary medium. Table 1 shows the instrument capabilities and fields of view (see Howard *et al.*, 2008, for more details).

The study period is at the declining phase of solar cycle 23 with very low level of solar activity (see Figure 1). This has the advantage of making unambiguous identification of the solar eruption associated with each type II radio burst. The type II bursts were well isolated and all but one originated from numbered active regions. The single exception is the type II burst on 26 April 2008 originating from an unnumbered active region. By playing Javascript

movies of EUV and white-light images, we were able to identify the EUV disturbances in the active region, followed by a white-light CME in the inner and outer coronal regions. The larger scale EUV disturbance is typically seen as a global wavelike phenomenon observed around the active region, distinctly larger than the bright flare loops or post-eruption arcades. The outermost part of the disturbance is often the EUV wave that surrounds the CME. The CME itself is occasionally observed in EUVI as a looplike structure that can be identified with the erupting flux rope subsequently observed in white light. Examples of such cases will be presented later. Each eruption is also identified with a soft X-ray flare, whose details can be found in the online SGD or NGDC flare archive. The heliographic coordinates of the soft X-ray flare in the active region serves as the solar source location of the eruption. We refer to the heliographic coordinates from Earth point of view (which is the same as for a spacecraft along the Sun – Earth line, such as SOHO).

Table 2 lists the metric type II bursts investigated in this paper. The date (yy/mm/dd format) and time range (hh:mm – hh:mm format) of the metric type II bursts are listed in columns 1 and 2, respectively. The starting (f_s) and ending (f_e) frequencies of the type II bursts are given in column 3. Note that the ending frequency usually means the burst reaching the lower frequency end of the dynamic spectrum. A question mark means we are not sure whether the emission is at the fundamental or harmonic of the plasma frequency. The drift rate (in MHz s^{-1}) in the metric range obtained from the dynamic spectra available at NGDC is given in column 4. When the type II burst continues to decameter – hectometric (DH) wavelengths, the ending time is given in column 5; N indicates no DH component. Only one (25 January 2007) type II burst had extended to the km domain. The speed of the CMEs as measured within the COR1 FOV (V_C, column 6) and LASCO FOV (V_L, column 7) is based on a linear fit to the height – time measurements in the respective FOVs. The CME width as measured in the LASCO FOV is given in column 8. The CME information in columns 7 and 8 are from the SOHO/LASCO CME catalog (cdaw.gsfc.nasa.gov) and is provided to make comparison with other studies of type II bursts in the pre-STEREO era. There were data gaps (DG) during only two of the ten type II bursts: There were no STEREO data except for a single EUVI and COR1 image for the 25 January 2007 event. The February 2007 type II occurred during a LASCO data gap. Fortunately, information is available in both cases from other coronagraphs. Details of the source region of the eruption such as the NOAA active region number, the GOES soft X-ray flare size, and the heliographic coordinates of the flare are given column 9. For example, the type II burst and CME on 25 January 2007 occurred in AR 0940 accompanied by a C6.3 flare from the location S08E90. An asterisk indicates that the source location was obtained from the previous location by applying solar rotation. The last column (10) gives the separation (in degrees) of STEREO Ahead (SA) and STEREO Behind (SB) with respect to Earth (E) and the separation between SA and SB. For example, at the time of the last event in Table 2 (26 April 2008 type II), SB was 24° behind Earth (BE) and SA was 25.6° ahead of Earth (AE), while SA and SB were separated by 49.6° (AB). The last column in Table 2 shows that the separation between the two STEREO spacecraft ranged from $\sim 0.5°$ to $\sim 50°$. The separation was large enough for the last few events to enable clear differences to be seen in the appearances of CMEs in the two views.

2.1. Statistical Results

Some important results can be derived from the information compiled in Table 2.

First, even though the solar activity is approaching its minimum (see Figure 1), type II bursts are still produced in all wavelength domains: purely metric, metric to DH (m – DH),

Table 2 List of metric type II bursts and the properties of CMEs.

Date	Time range	$f_e - f_s$ (MHz)	df/dt (MHz s^{-1})	DH II	V_C (km s^{-1})	V_L (km s^{-1})	W (degrees)	AR flare location	BE AE AB (degrees)
07/01/25	06:47 – 06:50	25 – 40	0.083	23:30	DG	1367	360	0940 C6.3 S08E90	0.16 0.39 0.55
07/02/19	00:18 – 00:21	30 – 45	0.2	N	186	DG	DG	0943 C1.1 S12E16	0.12 0.80 0.92
07/05/19	12:52 – 13:18	38 – 167?	0.25	13:05	1624	958	106	0956 B9.5 N07W06	2.1 5.9 8.0
07/05/22	14:36 – 14:55	25 – 82?	0.05	N	356	544	108	0956 B3.9 N02W42*	3.1 6.0 9.1
07/05/23	07:22 – 07:33	25 – 180	0.07	N	609	679	90	0956 B5.3 N02W55*	3.2 6.0 9.2
07/06/03	09:32 – 09:42	28 – 84	0.15	09:54	491	467	71	0960 C5.3 S08E67	3.9 7.1 11.0
07/08/06	09:16 – 09:21	25 – 94?	0.08	N	333	379	66	966 C1.5 S05E41	9.8 13.5 23.3
07/12/31	00:53 – 01:11	30 – 118?	0.11	01:23	771	995	164	0980 C8.3 S08E81	22.8 21.2 44.0
08/03/25	18:52 – 19:00	25 – 60	0.07	19:20	773	1103	90	0989 M1.7 S13E78	23.7 23.5 47.2
08/04/26	14:12 – 14:22	25 – 45?	0.024	14:15	335	515	281	?? B3.8 N08E09	24.0 25.6 49.6

and metric to kilometric (m – km). The average speed of the CMEs within the LASCO FOV is 779 km s^{-1}, considerably larger than that of the general population of CMEs ($\sim$ 480 km s^{-1}; see Gopalswamy, 2006a). The width of the CMEs within the LASCO FOV is also $\geq 66°$. Such speeds and widths are consistent with the fact that CMEs associated with type II bursts are generally more energetic. CMEs associated with purely metric type II bursts have an average speed of 534 km s^{-1}. However, the five m – DH type II bursts are associated with CMEs with a higher average speed (808 km s^{-1}). Finally, the single m – km type II burst on 25 January 2007 was associated with the fastest CME in Table 2 (1367 km s^{-1}). Despite the small sample, the type II bursts are consistent with the hierarchical relationship between CME kinetic energy and the wavelength range over which the type II bursts occur (Gopalswamy *et al.*, 2005, 2008a, 2008b; Gopalswamy, 2006b).

Second, the flare sizes are generally low: four B- and five C-class flares and a single M-class flare. Thus, 9 out of the 10 flares (or 90%) were of B and C class. This is in stark contrast to the energetic CMEs involved in the events. Such weak flares are problematic to the non-CME shock origin because the flare thermal energy is typically an order of magnitude smaller than the CME kinetic energy.

Third, there is a clear increase in CME speed between the inner and outer corona as measured in SECCHI/COR1 and LASCO FOVs. This is an indication that the CME is accelerating at the time of the metric type II burst. This result has important implications for the behavior of the drift-rate spectrum of type II bursts (Gopalswamy, 2006b). The exceptions are the two impulsive events, in which the speed started declining around the time of the metric type II burst. Considering the fact that CMEs liftoff from rest, these two events indicate that the CMEs reached peak speed even before the start of the type II bursts. A detailed analysis of the speed variation will be performed for several events in the next section.

3. Height – Time Analyses

One of the main objectives of this study is to determine the CME distance at the time of the type II burst onset. Six of the 10 metric type II bursts had CME observation when the burst was in progress, thus allowing us to obtain the height of the CME leading edge at the time of the burst onset accurately. In this section we describe a few such events with height – time plots and CME images. In particular, we consider the limb events because they are not subject to projection effects. The height – time analysis includes data from STEREO and SOHO. In STEREO, we use the SECCHI/EUVI images to track the earliest disturbances associated with the eruption. These are the disturbances that surround the rising CME, which could be EUV waves or shocks depending on the CME speed. The SECCHI/COR1 images provide CME height – time information in the crucial region where metric type II bursts originate. In the outer corona, CMEs are imaged using SECCHI/COR2 and SOHO/LASCO. Data from SA and SB are distinguished. Thus, there are generally three sets of data points (SA, SB, and SOHO) for each CME. When the spacecraft separation was not large, all three sets yield nearly identical results. At large separations, the three data sets give results consistent with the projection effects. In addition, one can also discern differences arising from the different fields of view.

3.1. The 31 December 2007 Event

Figure 2 illustrates the height – time analysis using the 31 December 2007 event. Throughout this paper, height means heliocentric distance, not height above the solar surface. The

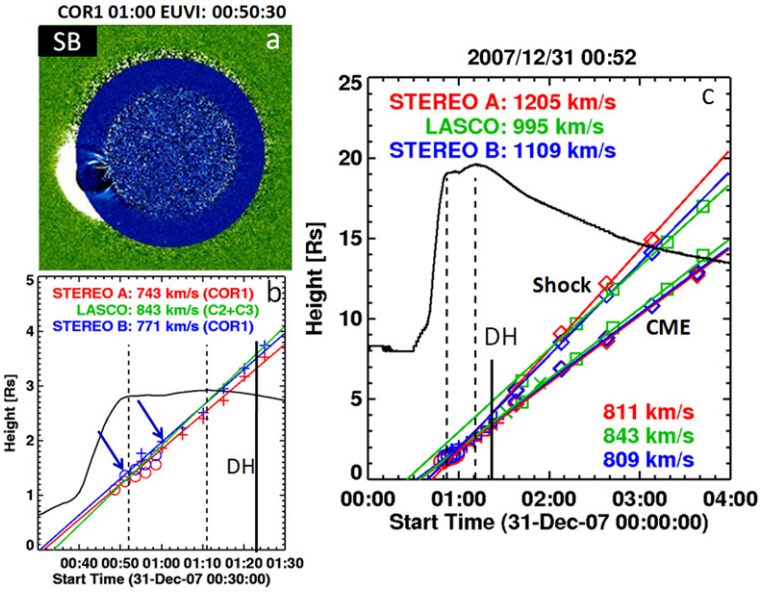

Figure 2 (a) COR1-B difference image at 01:00 UT superposed on the EUVI 171 Å difference image at 00:50:30 UT showing the 31 December 2007 CME associated with the metric type II burst at 00:52 UT. The blue annulus is the occulting disk seen above the EUVI limb. (b) Height – time plots of the CME from COR1 and EUVI data. STEREO Ahead (SA), STEREO Behind (SB), and SOHO data are color coded as red, blue, and green, respectively (with color coding applying to both symbols and lines). Thus red and blue "plus" symbols correspond to COR1 measurements from SA and SB, respectively. Similarly, red (SA) and blue (SB) circles represent EUVI measurements. The green line is the extrapolation of the SOHO/LASCO measurements made outside the COR1 FOV. The blue arrows point to the measurements from the EUVI and COR1 images shown in (a). The two vertical dashed lines mark the start and end times of the metric type II radio burst. The vertical solid line marked "DH" denotes the time when the type II burst at DH wavelengths ended (01:23 UT). (c) Height – time plots of the CME extended to include SOHO and STEREO FOVs. Measurements from the outer coronagraphs (C3: squares, COR2: diamonds) are distinguished from those of inner coronagraphs (COR1: plus symbols, LASCO/C2: crosses). The circles represent EUVI measurements as in (b). The GOES soft X-ray light curve in the 1 – 8 Å channel is superposed on the height – time plot for reference. The height – time plots corresponding to the main body of the CME and the diffuse feature (Shock) ahead of the CME are distinguished.

height – time measurements were made at the fastest moving segment of the CME. The CME can be seen above the southeast limb in COR1 and EUVI images (Figure 2a). The EUVI image shows both the looplike main body of the CME as well as disturbances on the sides. The dark crescent-shaped feature just above the limb is the CME leading edge in the previous frame, seen here as dark because of the running difference.

Figures 2b and 2c show the height – time history of the CME within the COR1 FOV and the entire FOV, respectively. Several height – time measurements were possible within the time interval of the metric type II burst (three EUVI and four COR1 data points; see Figure 2b). The EUVI image taken about a minute before the start of the type II burst (see Figure 2a) gives the overall initial extent of the shock. Note that the type II burst ended at DH wavelengths just before the CME left the COR1 FOV. The linear fits to the height – time plots are all close to each other, with an average speed of ~ 820 km s^{-1}. This is because the CME originated close to the limb in the view of all three coronagraphs. As Table 2 shows, the separation between SA and SB is $\sim 44°$; SA was $\sim 21°$ ahead of Earth, while SB was $\sim 23°$ behind. From Earth view, the eruption occurred at S08E81. As viewed from SA and SB,

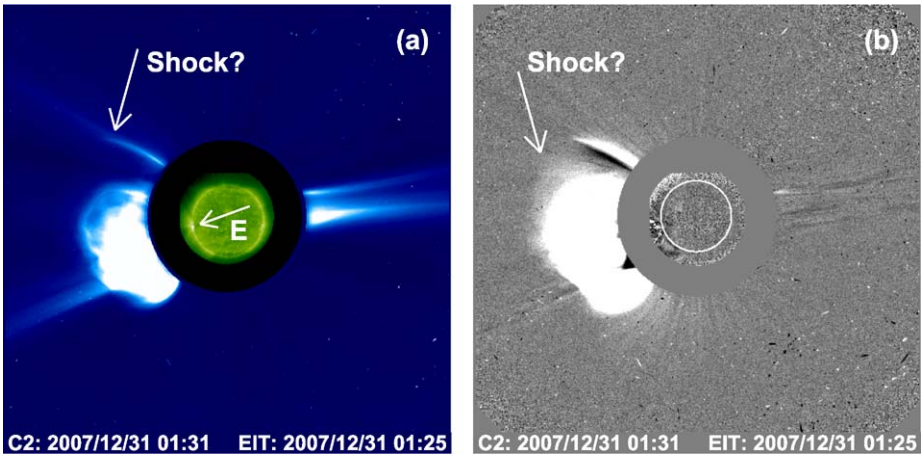

Figure 3 (a) LASCO/C2 image of the 31 December 2007 CME at 01:31 UT from the eruption center (E) at the east limb. The kink in the streamer to the north of the CME is indicative of the shock. (b) Difference image of the same CME showing diffuse filling of material up to the "kink." The diffuse structure marked "Shock?" extends from the nose and corresponds to the outermost disturbance. The disturbance can also be seen in the SOHO/EIT difference image superposed on the LASCO image. The LASCO image was taken slightly after the end of the type II burst.

the source longitude is expected to be E102 and E58, respectively. Thus the SA and Earth views of the CME were almost devoid of projection effects. The projection effects were also minimal for the SB view. Figure 2c shows an extra set of lines (marked "Shock") with data points only from the outer coronagraphs. These measurements correspond to the diffuse outer portion of the CME, which is likely to be the leading shock. The diffuse structures became visible when the CME reached a height of $\sim 5R_s$. Figure 3b shows a snapshot from SOHO/LASCO, which shows the diffuse structure (pointed by an arrow). Similar diffuse structure was also observed in the COR2 FOV (not shown). Diffuse structures like this have been reported in association with fast and wide CMEs that are radio quiet (Gopalswamy *et al.*, 2008b; Michalek, Gopalswamy, and Xie, 2007). It is possible that these shocks are weak and start separating from the driving CME as the CME slows down in the near-Sun IP medium. In the COR1 image shown in Figure 2a, it is difficult to see any diffuse structure at the leading edge, which suggests that the shock is close to the CME leading edge and cannot be seen distinctly. However, such diffuse structure can be seen at the flanks of the CME.

3.1.1. CME Height at Metric Type II Onset

The metric dynamic spectrum is rather complex. The type II starts with a fundamental – harmonic structure at 00:52 UT with the harmonic band showing band-splitting. The fundamental and harmonic components seem to continue into the S/WAVES and WAVES frequency range as shown in Figure 4. The fundamental component is somewhat weak in the metric domain. Both the fundamental and harmonic components end around 01:23 UT in the S/WAVES dynamic spectrum. An additional metric type II burst (marked 2) with a different drift rate seems to be superposed on the first one (see Figure 4 around 01:05 UT). The GOES time profile also shows two peaks, the second one coinciding with the second episode of type II burst. The DH type III bursts also start only during the second episode. Since there is no other eruption from other regions, we think the two episodes of type II bursts are from

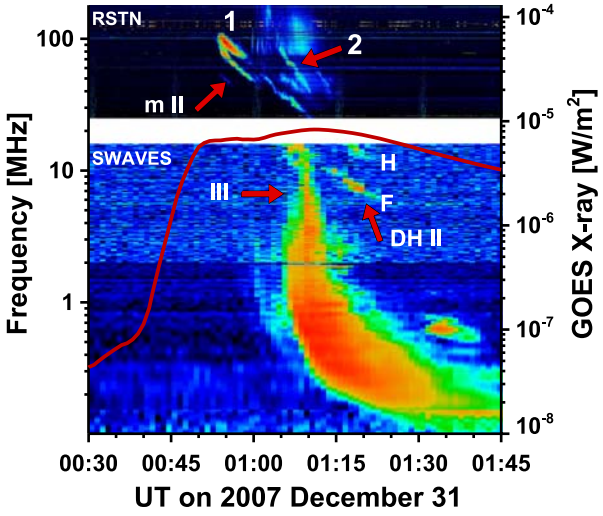

Figure 4 Composite dynamic spectrum showing the metric type II burst (m II) observed at the Learmonth Observatory belonging to the Radio Telescope Network (RSTN) and the DH type II burst (DH II) observed by STEREO/WAVES (S/WAVES) on 31 December 2007. The GOES time profile shows two peaks. There seem to be two episodes (marked 1 and 2) of the metric type II burst, with the second one being brief with fundamental – harmonic (F – H) structure. The DH II shows F – H structure, which is a continuation of the first metric type II episode (marked 1). The DH type III burst is marked as "III." The fundamental components of the type II in metric and DH domains are indicated by arrows.

the same eruption. It is possible that the shock encounters a dense streamer and produces the second episode. It is also possible that, early in the eruption, the flare-accelerated electrons did not have access to the open field lines, and hence there are no type III bursts.

The height – time plots in Figure 2 show that, at the time of the metric type II burst onset, the location of the CME leading edge was at $1.32R_s$, $1.46R_s$, and $1.39R_s$, respectively, from the SA, SB, and SOHO data. These heights are very close to each other and smaller than the average height of $\sim 2.2R_s$ obtained using LASCO data alone (Gopalswamy *et al.*, 2005). We conclude that the heliocentric distance of the shock is not too different from $\sim 1.46R_s$. When the DH type II burst ended at 01:23 UT, the CME was at a height of $\sim 3.5R_s$. This means the shock was able to accelerate electrons to sufficient numbers only over a short distance of $\sim 2R_s$. In the following, we attempt to explain why this is so.

3.1.2. CME Speed Evolution and Cessation of Type II Burst

Since there are sufficient numbers of height – time measurements in each view, we were able to follow the evolution of the CME speed in time. We combined the measurements at various distance ranges in each view (SA, SB, and SOHO). From STEREO data, the first data point is from EUVI, the next four are from COR1, and the last two are from COR2. In LASCO data, the first speed measurement is from C2 and the rest are from C3. The speeds were determined by fitting a straight line to four successive height – time data points. Figure 5 shows the CME speed as a function of heliocentric distance and time for the 31 December 2007 event. We see that the speed increases from ~ 475 km s^{-1} near the start of the type II burst, reaches a maximum value of ~ 950 km s^{-1} at $\sim$ 01:15 UT, and then declines. The maximum speed reached is slightly different as measured in SA (888 km s^{-1} at $3.0R_s$) and SB (941 km s^{-1} at $3.1R_s$). The difference in peak speeds ($\sim 7\%$) is not significant because

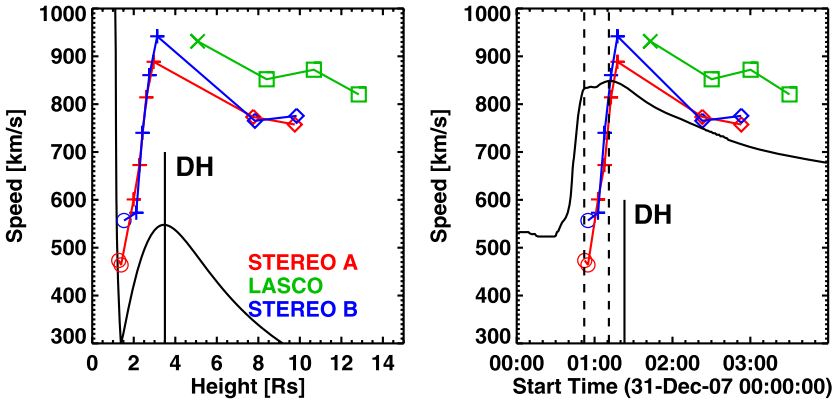

Figure 5 (Left) Variation of the CME speed for the 31 December 2007 event as a function of height derived from the height – time plots in Figure 2. Variation of the Alfvén speed as a function of height (black curve) is superposed on the plot. (Right) Variation of the CME speed as a function of time. The GOES soft X-ray light curve is superposed on the speed – time plot. The interval of the metric type II burst is marked by the two vertical dashed lines. The end of the DH type II burst is indicated by the solid vertical line marked "DH." Note that the type II emission ends immediately after the speed starts decreasing from its maximum value ($\sim 950\ \mathrm{km\,s^{-1}}$). The speed reaches its maximum value when the CME is at a height of $3R_s$. The speed profile peaks slightly after the flare peak, which is different from the usual scenario.

the position angle at which the CME leading edge was tracked is slightly different for SA and SB. Note that there was no COR1 speed measurement after the peak, so the peak value is only approximate. Judging by the C2 data point, it is possible that the speed reached a slightly higher value before declining. In the declining part, the speed measurements are available only from COR2 (two data points) and LASCO (four data points). LASCO speeds are slightly higher, but only by about 10%.

By the time the type II burst ended at 01:23 UT, the CME was still fast, with speed $> 800\ \mathrm{km\,s^{-1}}$. The speed had declined only to $\sim 800\ \mathrm{km\,s^{-1}}$ by the time the CME reached the edge of the LASCO/C3 FOV. When the CME was moving with a speed of $\sim 500\ \mathrm{km\,s^{-1}}$, it was associated with a type II burst, but not when it was moving as fast as $800\ \mathrm{km\,s^{-1}}$. To understand this contradiction, we need to look at how the characteristic speed of the ambient medium (magnetosonic speed or Alfvén speed) changes with height. In the core of active regions, the characteristic speed is high (more than $1000\ \mathrm{km\,s^{-1}}$), but it drops rapidly in the outskirts of the active region to $\sim 300\ \mathrm{km\,s^{-1}}$. The characteristic speed again starts rising, reaching a maximum around $550\ \mathrm{km\,s^{-1}}$ (Mann *et al.*, 1999; Gopalswamy *et al.*, 2001a) in the height range $3R_s - 4R_s$. In Figure 5, we have overlaid the radial profile of the Alfvén speed (V_a) computed using the Saito, Poland, and Munro (1977) density model as in Gopalswamy *et al.* (2001a), except that we have used V_a instead of the magnetosonic speed. The radial evolution of the characteristic speed is somewhat parallel to that of the CME speed except in the core of the active region. Near the start of the type II burst, the Alfvénic Mach number is ~ 1.7 (556/329 in EUVI-B). When the CME reaches its peak speed, the Mach number remains the same (941/542 in COR1-B). It is interesting that the type II burst ends when the CME speed starts declining (see Figure 5). When the type II burst ended, the CME speed was somewhere between 850 and 900 $\mathrm{km\,s^{-1}}$ and the Alfvén speed has reached its maximum value ($\sim 550\ \mathrm{km\,s^{-1}}$), suggesting that the Mach number is in the range 1.5 – 1.6. The Mach number is expected to be even lower, when the solar wind speed, which begins to become significant around $3R_s$, is taken into account (see, *e.g.*, Sheeley *et*

al., 1997; Gopalswamy *et al.*, 2001a). A shock with such a low Mach number is likely to be a subcritical shock and hence the particle acceleration efficiency is expected to be low (Mann *et al.*, 2003). Consequently, a sufficient number of electrons required to produce a type II burst may not be accelerated by the weak shock. The combination of the characteristic speed of the medium and the CME speed seem to be such that the shock either became too weak or decayed by the time the CME reached the outer corona. It is worth noting that the peak V_a shown in Figure 5 is only a representative value, which can be much higher or lower depending on the actual density and magnetic field in the corona. Furthermore, the solar wind speed reaches about 150 km s^{-1} at $\sim 5R_s$ (see Sheeley *et al.*, 1997), so shock-driving gets more difficult because the solar wind speed needs to be subtracted from the CME speed before comparing with V_a to get the Mach number. Thus, CME speed decrease and solar wind speed increase weaken the shock, while the decreasing Alfvén speed makes the shock stronger. The combination of the three speeds decides the existence and the strength of the shock.

3.2. The 25 March 2008 Event

In many ways the 25 March 2008 event is similar to the 31 December 2007 event: It is an east-limb CME with an m – DH type II radio burst and the shock component was discernible after the end of the DH type II burst. Even the morphology of the CME in EUVI and COR1 images is nearly identical to that of the 31 December 2007 CME. The EUVI 171 Å image in Figure 6a shows the curved-front CME with extended disturbances near the limb on the northern and southern edges and on the disk. This is the EUV disturbance that surrounds the CME. The image in Figure 6a was obtained only a minute after the start of the type II burst and demonstrates that the shocks can form very close to the Sun. The leading edge of the EUVI CME is at a height of $1.47R_s$. In the minute before the start of the type II burst, the EUVI CME was at a height of $1.3R_s$. Thus the CME was somewhere between $1.3R_s$ and $1.47R_s$ when the type II burst started. The COR1 image shown in Figure 6a was taken ~ 1.5 minutes after the superposed EUVI image, so the CME is slightly larger in size. The height – time plots in Figure 6 give a CME leading edge height of $1.42R_s$, consistent with the EUVI observation. From Earth view, the CME occurred at S13E78, so it is slightly on the disk in the SB view because SB was $\sim 24°$ behind Earth at the time of the eruption. Similarly, the CME was slightly behind the limb for SA, which was $\sim 24°$ ahead of Earth, so the CME leading edge at the time of the type II was at $1.56R_s$. The nearest SA image in EUVI was at 18:51 UT, one minute before the type II onset, and showed the CME leading edge to be at $1.50R_s$. Thus, a height of $\sim 1.5R_s$ for the CME leading edge at the time of type II burst onset is a good estimate. The SOHO/LASCO observations give a leading edge height of $1.65R_s$ at the type II onset, which is substantially higher than the STEREO values. This is mainly because the average speed in the LASCO FOV is relatively higher (1037 km s^{-1}; see Figure 6b). At first appearance (at 19:31 UT; see Figure 7) in the LASCO FOV, the CME was already at a height of $5.79R_s$, requiring too much extrapolation to the time of type II onset. As we showed for the 31 December 2007 event, the CME speed varies significantly between the CME liftoff and its appearance in the LASCO FOV, which is not captured in LASCO observations.

The *Wind*/WAVES dynamic spectrum for the 25 March 2008 event is shown in Figure 7 along with the LASCO image when the CME first appeared. An EUV difference image obtained by SOHO/EIT at 19:25 UT is also shown superposed on the LASCO image. The extent of the EUV disturbance closely matches the outermost disturbance in white light. Such comparisons were previously made by Thompson *et al.* (2000), who concluded that

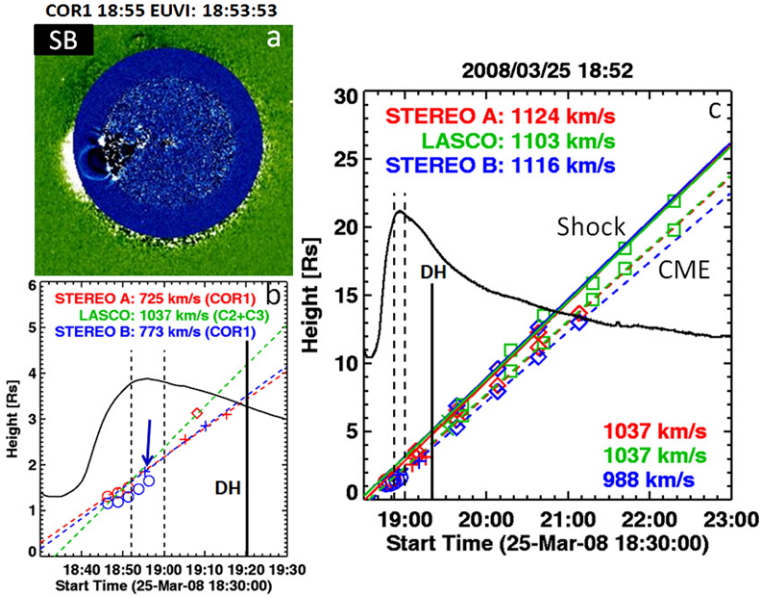

Figure 6 (a) COR1-B difference image at 18:55:23 UT superposed on the EUVI 171 Å difference image at 18:53:53 UT showing the 25 March 2008 CME when the metric type II burst was in progress. (b) CME height – time plot within the COR1 FOV with EUVI and COR1 data points. The symbols have the same meaning as in Figure 2. The arrow points to the COR1 and EUVI measurements from the images shown in (a). The two vertical dashed lines mark the start and end times of the metric type II radio burst. The vertical line marked "DH" denotes the time when the type II burst at DH wavelengths ended (19:20 UT). (c) Extended height – time plots from SOHO and STEREO, with the symbols and colors having the same meaning as in Figure 2. The GOES soft X-ray light curve in the 1 – 8 Å channel is superposed on the height – time plot for reference. The height – time plots in dashed and solid lines correspond to the main body of the CME and the shock as labeled.

the extended dimming areas mapped out the apparent "footprint" of the CME. Here we note that the CME can be seen as a distinct flux rope structure and the outermost white-light disturbance can be traced above the flux rope as a diffuse feature, which is likely to be the sheath of the CME-driven shock. The flux-rope structure, the outermost sharp feature in Figure 7, is clearly confined to the central portion of the EUV disturbance, suggesting that the flux rope is the driver of the EUV wave. As in the case of the 31 December 2007 event, the shock was not seen distinctly ahead of the COR1 CME (but disturbance was seen at the sides low in the corona). The leading diffuse feature can be seen only in the outer corona, also after the end of the DH type II burst. This suggests that the shock is getting decoupled from the CME because it gets weaker. Note that the DH type II burst ends at 19:20 UT, which is even before the CME appeared in the LASCO FOV. The lowest frequency of the type II burst that appears as the continuation of the metric type II burst was ~ 10 MHz. From the height – time plot in Figure 6b we see that the CME leading edge was at a height of $\sim 3.6R_s - 3.7R_s$ when the type II burst ended at 10 MHz.

Figure 8 shows that the CME speed increases rapidly when the metric type II burst is in progress. Unfortunately, there is no CME observation between the end of the metric type II and the end of the DH type II. But the shape of the speed profile suggests that the speed should have peaked somewhere before the end of the DH type II burst. Since the speed profile is expected to be similar to that of the GOES soft X-ray profile (Zhang *et al.*, 2001), it is

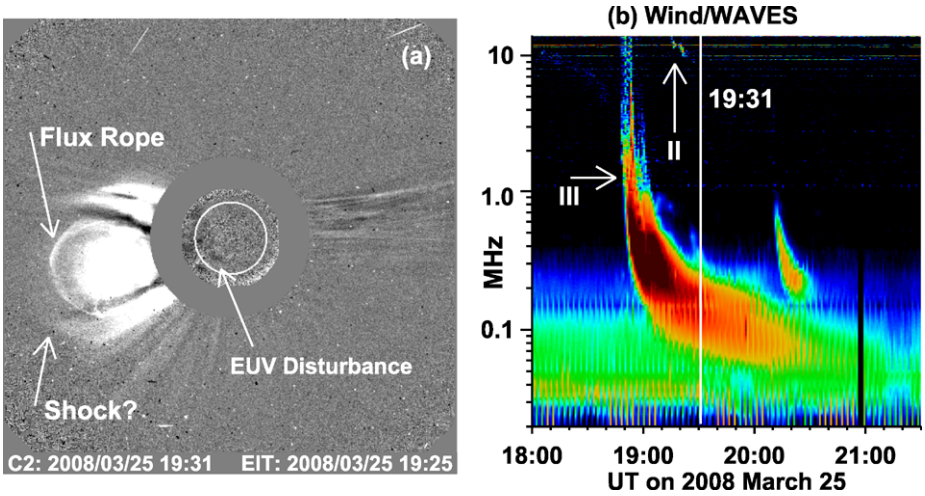

Figure 7 (a) The 25 March 2008 CME when it first appeared in the LASCO/C2 FOV. The CME had a flux rope structure (marked) and a leading diffuse feature, whose outermost edge we interpret as the shock. The EUV disturbance seen above the limb and on the disk coincides with the outermost part of the white-light disturbance that surrounds the flux rope. (b) *Wind*/WAVES dynamic spectrum with the type III and type II bursts marked. The vertical line marks the time (19:31 UT) of the LASCO frame on the left.

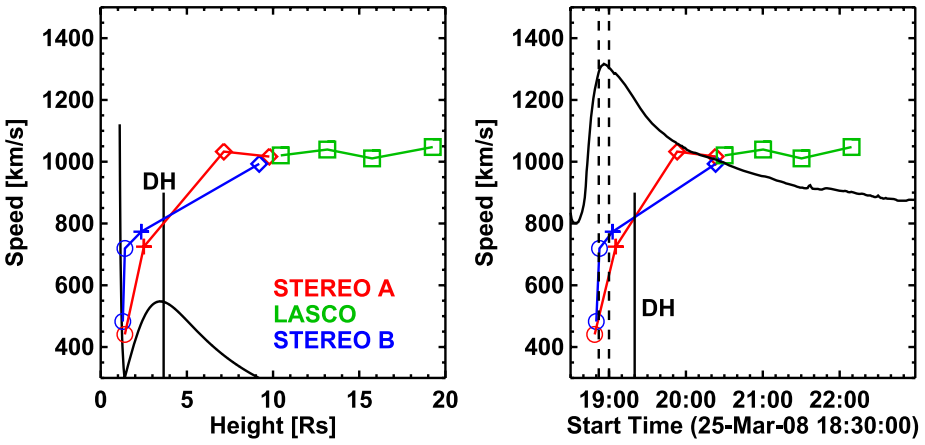

Figure 8 Variation of the CME speed with height (left) and time (right) for the 25 March 2008 CME. The duration of the metric type II burst (vertical dashed lines) and the end of the DH type II burst (solid vertical line) are marked. The Alfvén speed profile is overlaid on the speed – height plot as in Figure 5.

likely that the CME speed peaked before the end of the DH type II burst. The end of the DH type II burst coincides with the distance at which V_a peaks, very similar to what happened in the 31 December 2007 event. The CME speed attained a constant value (~ 1000 km s^{-1} in SA, SB, and SOHO) after the end of the type II burst. This speed is higher than that when the metric type II was in progress (~ 800 km s^{-1}). This means the peak CME speed must have been above 1000 km s^{-1}. The lack of type II burst beyond 19:20 UT even with a CME speed of ~ 1000 km s^{-1} suggests that the Alfvén speed in the ambient medium is close to 1000 km s^{-1} or only slightly smaller, making the shock too weak to produce the type II

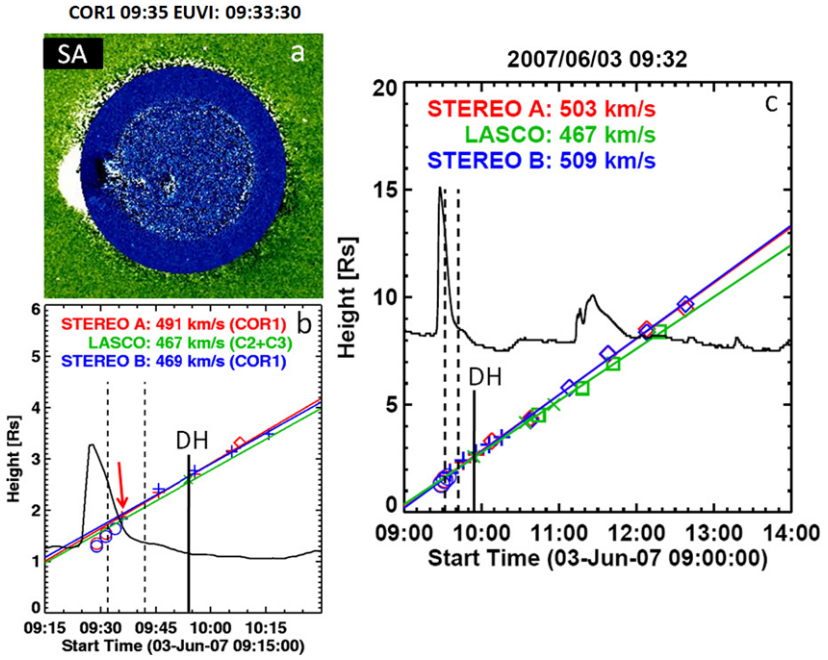

Figure 9 (a) COR1-A difference image at 09:35:18 UT superposed on the EUVI 171 Å difference image at 09:33:30 UT showing the 3 June 2007 CME when the metric type II burst was in progress. (b) Height – time plots of the CME within the COR1 FOV. The arrow points to the data point corresponding to the COR1 image in (a). Times of metric type II (between the dashed lines) and the end of DH type (vertical solid line at 09:54 UT) are marked. (c) CME height – time plots from SOHO and STEREO, with the symbols and color having the same meaning as in Figure2. The GOES soft X-ray light curve in the 1 – 8 Å channel is superposed on the height – time plot for reference. The metric type II duration and the end time of DG type II are shown as in (b).

burst. The tenuous-looking corona between the two streamers (see Figure 7) into which the CME was launched may have had a higher characteristic speed than the 550 km s^{-1} indicated by the V_a profile in Figure 8. The metric type II burst itself might have come from the flanks of the CME, where the streamers are located. When the shock traverses through the streamers, it encounters lower Alfvén speed and higher Mach number. Once the shock crosses the streamer region in the lateral direction, the shock enters into a higher Alfvén speed region, rendering the shock very weak and consequently ending the metric type II burst. In summary, the 25 March 2008 event is consistent with the interpretation provided for the better observed 31 December 2007 event.

3.3. The 3 June 2007 Event

The metric type II burst on 3 June 2007 was associated with an east-limb CME and a C5.3 flare from AR 10960 located at S08E67. The separation between SA and SB was only $\sim 11°$, so the eruption was a limb event for all three views. Accordingly, the CME appeared nearly the same as viewed by STEREO and SOHO (see Figure 9 for nearly identical height – time plots). The metric type II burst lasted for $\sim$ 10 minutes, starting at 09:32 UT and ending at 09:42 UT. The *Wind*/WAVES dynamic spectrum showed a faint and thin slanted feature, which seems to be a continuation of the harmonic component of the metric type II burst.

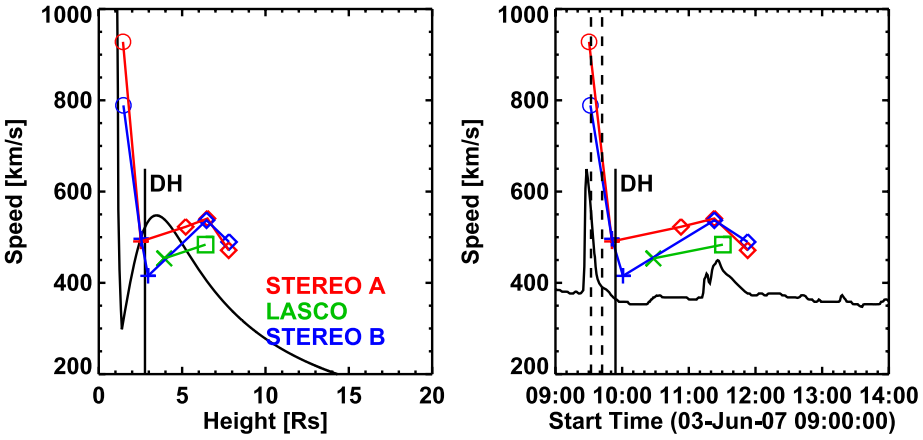

Figure 10 CME speed as a function of height (left) and time (right) for the 3 June 2007 event. The GOES soft X-ray light curve and the duration of the metric of type II burst (two vertical dashed lines) are also shown. The vertical solid line marks the end of the DH type II burst. The Alfvén speed profile is shown in the left panel (black curve).

The DH component continued down to ~ 3 MHz and ended at 09:54 UT. There was only one COR1 image each from SA and SB during the metric type II burst, but there were several images outside the type II interval. Figure 9a shows a EUVI – COR1 composite image from SA showing the CME at a height of $1.87R_s$ and overlying the eruption in EUV. The corresponding CME in SB was at a height of $1.83R_s$ (09:36 UT). The height – time plots give the CME height as $1.66R_s$, $1.6R_s$, and $1.65R_s$ as obtained from SA, SB and SOHO, respectively. The eruption is closest to the limb in the view from SA, so we can say that the CME leading edge was at a height of $\sim 1.66R_s$ when the type II burst started. The GOES soft X-ray plot superposed on the height – time plot shows that the flare was extremely impulsive, lasting only ~ 8 minutes. There were two EUVI images of the eruption well before the start of the type II burst. When the speed was computed as a function of time, we found something remarkable: The CME speed had already reached its peak when the type II burst started (see Figure 10). The peak speed also coincided with the peak of the soft X-ray flare. The peak CME speed was ~ 925 km s^{-1} (SA) near the start of the metric type II burst and dropped to ~ 500 km s^{-1} when the type II burst ended at 09:54 UT in the DH domain. The speed evolution closely followed the impulsive soft X-ray profile and dropped below the local V_a when the type II burst ended. In this case, the shock itself should have disappeared, whereas in the previous cases the shocks weakened and became subcritical. In contrast to the previous events, the type II burst ended even before V_a reached its peak value. The CME first appears in the LASCO/C2 FOV with its leading edge at $2.6R_s$ when the type II burst just ended at 3 MHz. Thus, the formation and disappearance of the shock were completed even before the CME appeared in the LASCO FOV.

3.4. The 25 January 2007 Event

The 25 January 2007 CME is the only event associated with a metric – kilometric type II burst. There was no metric type II burst reported in the SGD, but when we examined the dynamic spectrum available at the NGDC, we found a weak type II feature in the interval 06:47 to 06:49 UT drifting from 40 to 25 MHz. The drift rate was ~ 0.1 MHz s^{-1}, which is

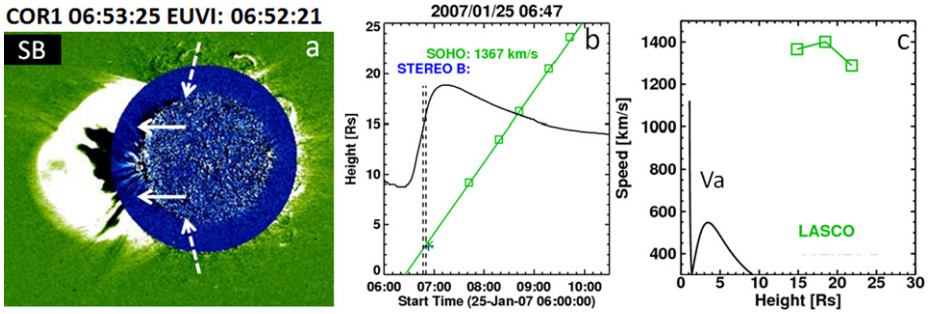

Figure 11 (a) COR1 image from SB showing the 25 January 2007 CME during its early phase (at 06:53 UT). The leading edge of the COR1 CME is at $2.85R_s$. The solid arrows point to the main body of the CME. The dashed arrows point to the outer edge of the EUV disturbance, coinciding with the outermost part of the CME-associated disturbance in white light. (b) CME height – time plot from SOHO/LASCO with the single data points from COR1 (plus symbol, corresponding to the image on the left) and LASCO/C2 (cross symbol). The GOES soft X-ray light curve and the interval of metric type II burst (shown by two vertical dashed lines) are overplotted for reference. (c) CME speed variation as a function of heliocentric distance with superposed Alfvén speed profile (V_a).

typical of metric type II bursts (Mann *et al.*, 1996). STEREO data coverage was very poor for this event with no SA observations and only one COR1 image in SB at 06:53 UT (see Figure 11a), which was taken after the metric type II burst. The EUVI image superposed on the COR1 image shows the EUV disturbance extending to the outskirts of the COR1 CME at the limb. The CME leading edge from COR1 (plus symbol on the height – time plot) is consistent with the first appearance time of the CME in the LASCO/C2 FOV with its leading edge at $\sim 2.98R_s$. The CME height – time plot is mainly from LASCO/C3 images with just single data points from COR1-B and LASCO/C2 (see Figure 11). The CME speed was obtained only from the LASCO data for this event. The high speed of the CME (1367 km s^{-1}) is consistent with the expected speed for an metric – kilometric type II burst (with the average speed of all such type II bursts being ~ 1500 km s^{-1}; see Gopalswamy *et al.*, 2005). The speed variation shown in Figure 11c is also consistent with the metric – kilometric type II burst because the CME speed is much larger than the Alfvén speed and hence must be driving a shock throughout the inner heliosphere.

The metric – kilometric type II burst drifted from 14 MHz and reached ~ 90 kHz by the end of the day (23:30 UT). In LASCO, the CME was tracked from $2.98R_s$ at 06:54 UT (when the CME first appeared in the LASCO FOV) to $27R_s$ at 10:20 UT (when the CME left the LASCO FOV). The corresponding frequencies are ~ 14 to ~ 0.5 MHz. Figure 12 shows the LASCO/C3 image of the CME at 08:18 UT and the *Wind*/WAVES dynamic spectrum. At this time, the CME leading edge had reached a heliocentric distance of $\sim 13.5R_s$ with the radio emission occurring at a frequency of ~ 0.9 MHz. Unlike the 31 December 2007 and 25 March 2008 events, we do not see the shock-like structure at the leading edge of the CME. This may be because the shock may still be close to the CME. However, we do see diffuse structure at the flanks (see Figure 12).

The significant overlap between the LASCO FOV and the plasma levels corresponding to the radio emission can be exploited to understand the relation between CME evolution and the type II burst in the IP medium. Since the shock is not seen distinctly from the CME leading edge, we assume that the CME height is approximately the same as the shock height. With this assumption, we see that the radio emission occurring at a frequency of ~ 500 kHz must come from a heliocentric distance of $\sim 27R_s$. Although there is no CME observation

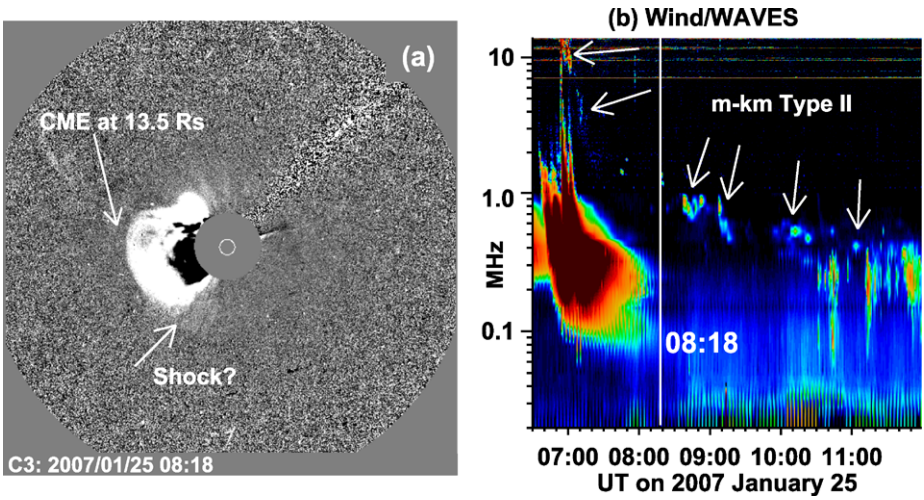

Figure 12 *Wind*/WAVES dynamic spectrum showing the meter – kilometer type II burst (b) and a snapshot (08:18 UT) of the associated CME from SOHO/LASCO (a). The type II burst is fragmented as indicated by the arrows. It is faint above 1 MHz because of the lower sensitivity of the WAVES instrument in this frequency range. The vertical white line marks the time (08:18 UT) of the LASCO frame on the left, which shows the frequency of the type II burst (~ 0.9 MHz) corresponding to the CME height ($13.5 R_S$). The faint shock-like feature is marked on the CME image.

beyond $32 R_s$, the radio emission continued to lower frequencies, which means the shock remained strong for another half a day or so when the radio emission reached 90 kHz.

The plasma density at a heliocentric distance of $27 R_s$ can be estimated from the frequency of type II burst because the radio emission takes place at the fundamental or harmonic of the local plasma frequency. For this we need to decide whether the observed burst is at fundamental or harmonic. Unfortunately, the burst does not have both the fundamental and harmonic components, so we need to resort to some models to determine the emission component. Here we use the Leblanc, Dulk, and Bougeret (1998) model for the variation of electron density as a function of heliocentric distance. First we obtained the frequency of emission at several discrete times when the radio emission is clear. Then we matched the CME heights to the chosen times from the CME height – time plot (see Figure 12). For these CME heights, we can obtain the electron density (and hence the emission frequency) in the IP medium using the Leblanc, Dulk, and Bougeret (1998) model. For each height we get two frequencies, one assuming fundamental emission and the other harmonic. We thus obtain frequency – time plots, which are overlaid on the dynamic spectrum in Figure 13. The model had to be multiplied by a factor of 1.7 to get the best fit to the observed variation of emission frequency with time. The multiplication factor is normally obtained by looking at the plasma density at 1 AU, but the present event was an east-limb event, so one has to wait for a week to obtain the solar wind density in the solar wind originating from the corona above the eruption region. Therefore, we have chosen a multiplication factor in an *ad hoc* manner. The frequency – time lines in Figure 13 show that the harmonic emission curve fits the observation quite well, so we conclude that the radio emission takes place at the harmonic of the plasma frequency. Thus at a heliocentric distance of $\sim 27 R_s$, the plasma frequency is ~ 250 kHz (corresponding to half the emission frequency), which gives a plasma density of ~ 772 cm^{-3}. We shall make use of the radial variation of the emission

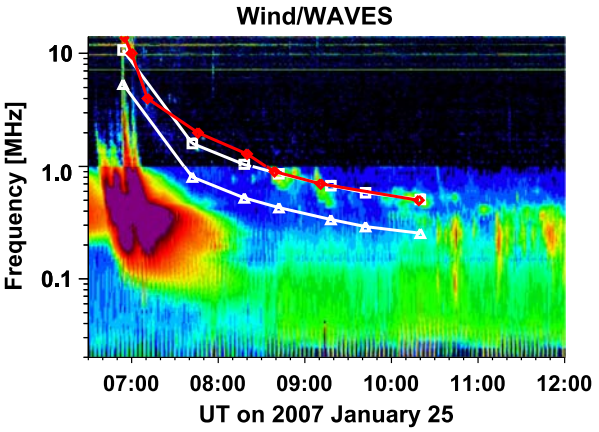

Figure 13 *Wind*/WAVES dynamic spectrum showing the type II burst with the fundamental (triangles) and harmonic (squares) frequencies derived from the Leblanc, Dulk, and Bougeret (1998) density model superposed. The diamond symbols mark the frequency – time data points from the dynamic spectrum that were used in obtaining the type II frequency corresponding to the leading edge of the CME.

frequency and the radial evolution of the CME speed to understand the drift-rate spectrum in Section 4.

3.5. Other Events

Among the six remaining events, the data coverage for the 19 February 2007 CME was very poor since there was a LASCO data gap and COR1 observed the CME only in two frames. Moreover, the COR1 frames were obtained after the metric type II burst ended. The speed computed from just two frames is not very accurate. Furthermore, the eruption was near the disk center (S12E16) for both SA and SB, so the measured speed is subject to large projection effects. All three events in May 2007 (19, 22, and 23) occurred in the same AR (NOAA 0956). The events of 19 and 22 May had COR1 images during the type II bursts. However, the eruption was on the disk (N07W06 and N02W42), so the measurements were subject to projection effects. The spacecraft separation was also not large enough to eliminate the projection effects. The 23 May event was closer to the limb, but unfortunately, the COR1 observations were not made until after the end of the type II burst. The 6 August 2007 CME was associated with an impulsive flare similar to the 3 June 2007 event discussed in Section 3.4. Unfortunately, there was no COR1 frame when the type II burst was in progress. Finally, the 26 April 2008 event had COR1 observations when the type II was in progress. However, the eruption was on the disk for all three views, so the height – time measurements are subject to projection effects.

The height – time plots of the three events with CME data in COR1 during the metric type II burst are shown in Figure 14. The plots show that the SA, SB, and SOHO plots are close to each other for the May 2007 events because the spacecraft separation was not large. However, the three plots are very different for the 16 April 2008 event because of the large spacecraft separation ($\sim 50°$): SA data yielded the highest speed (676 km s^{-1}) because the source location from SA was N08E33 and the projection effects are expected to be modest. For SB, the speed is the smallest (417 km s^{-1}) because the source location from SB view is N08W15. The SOHO view had the source location at N08E09, so the speed should be similar to the SB view. However, the speed is slightly higher (515 km s^{-1}) because SOHO data points correspond to a larger height, thus missing the acceleration phase of the CME. The three views to the 26 April 2008 CME can be used to get the deprojected (space) speed of the CME, but that is beyond the scope of this paper.

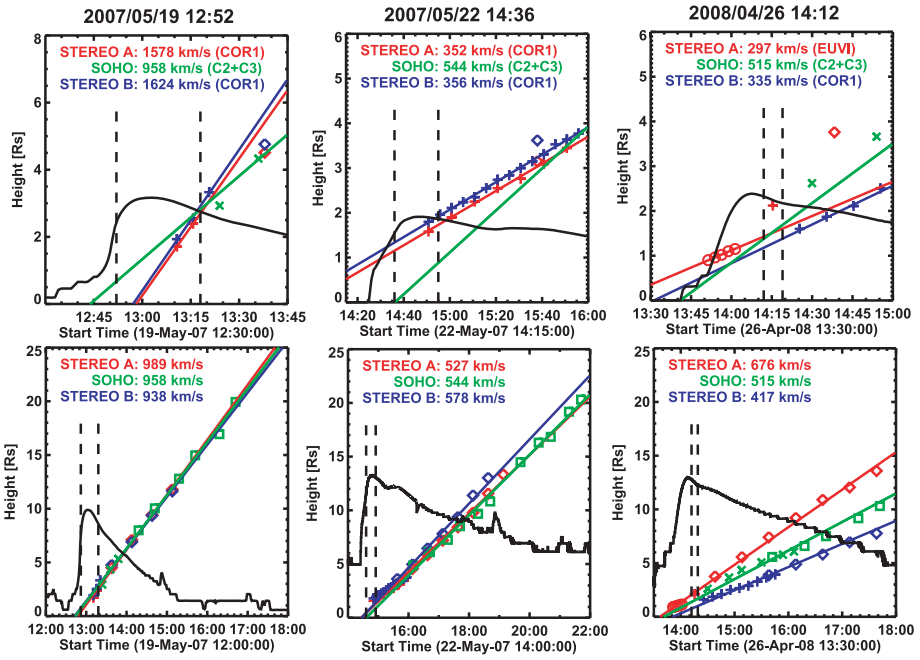

Figure 14 CME height – time plots for the events on 19 and 22 May 2007 and 26 April 2008 within the COR1 FOV (top row) and the entire FOV (bottom row). For the 26 April 2008 event, there is only one COR1-A data point, so we have given the speed obtained from EUVI data in the top panel. The GOES soft X-ray light curve in the 1 – 8 Å channel and the interval of metric type II radio burst (between the two vertical dashed lines) are shown for reference.

4. The Universal Drift Rate Spectrum

We now discuss how the observational results just presented can be used to understand the universal drift-rate spectrum of the type II bursts over the entire range of frequencies over which type II radio bursts occur. It has been known for a long time that the starting frequency and drift rate of metric type II bursts are well correlated (see, *e.g.*, Mann *et al.*, 1996; Vršnak *et al.*, 2002). When extended to the longer wavelength domain, the correlation remained high (correlation coefficient > 0.8). In fact over the entire frequency range of type II radio bursts in the inner heliosphere, it was found that measured drift rate ($\mathrm{d}f/\mathrm{d}t$) is related to the emission frequency (f) by a power law (Vršnak *et al.*, 2001; Aguilar-Rodriguez *et al.*, 2005):

$$|\mathrm{d}f/\mathrm{d}t| \sim f^{\epsilon}, \tag{1}$$

where $\epsilon \sim 2$ is the observed power-law index. The power law in Equation (1) is valid over six orders of magnitude in emission frequency and has been shown to be true even when observations from various instruments, spectral domains, and epochs are combined (Aguilar-Rodriguez *et al.*, 2005). This is the reason we call relationship (1) the universal drift-rate spectrum.

Assuming that the type II radio emission occurs at the local plasma frequency (f_{p}), one can relate the speed of the disturbance away from the Sun to the drift rate of the type II burst if we know how the density (n) falls off with distance (r) from the Sun, where the radio

emission occurs. The plasma frequency is related to the plasma electron density as

$$f_{\rm p}(r) = 9 \times 10^{-3} \sqrt{n(r)}, \tag{2}$$

where $f_{\rm p}$ is in MHz and n is in cm^{-3}. If we take the electron density variation with r as a power law, $n(r) \sim r^{-\alpha}$, we see that

$$f_{\rm p}(r) \sim r^{-\alpha/2}. \tag{3}$$

For fundamental plasma emission, the emission frequency $f = f_{\rm p}$, so the radio emission occurs progressively at lower frequencies at later times. Thus one can write the frequency drift rate as

$$\mathrm{d}f/\mathrm{d}t = (\mathrm{d}f/\mathrm{d}r)(\mathrm{d}r/\mathrm{d}t). \tag{4}$$

Note that $\mathrm{d}r/\mathrm{d}t = V$ is the speed of the shock moving away from the Sun down the density gradient. In principle the density gradient (or plasma frequency gradient) may be in a different direction than the direction of the disturbance. Here we assume that they are in the same direction. Using Equation (2) and the relation $f = f_{\rm p}$, we can write

$$\mathrm{d}f/\mathrm{d}r = (f/2n)(\mathrm{d}n/\mathrm{d}r) = (f/2Ln), \tag{5}$$

where $Ln = [(1/n)(\mathrm{d}n/\mathrm{d}r)]^{-1}$ is the density scale height in the medium through which the shock propagates. Combining Equations (4) and (5), we can get the shock speed as

$$V = 2Ln(1/f)(\mathrm{d}f/\mathrm{d}t). \tag{6}$$

Measuring the drift rate from the dynamic spectrum and obtaining the density scale height from a density model, one can get the shock speed. The speed of the shock can also be obtained from the $2f_{\rm p}$ (second harmonic emission) in a similar fashion.

To understand the observed variation of $\mathrm{d}f/\mathrm{d}t$ with f, we need to consider Equation (4) together with Equation (3). We can rewrite Equation (4) as

$$\mathrm{d}f/\mathrm{d}t = (Vf/2n)(\mathrm{d}n/\mathrm{d}r), \tag{7}$$

which upon substituting for f and n from Equation (3) can be written as

$$|\mathrm{d}f/\mathrm{d}t| \sim Vr^{-1-\alpha/2}. \tag{8}$$

Note that Equation (7) needs to be modified for harmonic emission ($f = 2f_{\rm p}$) and when a non-power-law distribution is used. Here we have used the absolute value of $\mathrm{d}f/\mathrm{d}t$ because it is negative for type II bursts (*i.e.*, the frequency of emission decreases with time). Writing r in terms of f from Equation (3), we get

$$|\mathrm{d}f/\mathrm{d}t| \sim Vf^{(\alpha+2)/\alpha}. \tag{9}$$

Assuming $\alpha = 2$, Vršnak *et al.* (2001) obtained $\mathrm{d}f/\mathrm{d}t \sim Vf^2$. Furthermore, if the shock speed does not change significantly ($V =$ constant), then

$$|\mathrm{d}f/\mathrm{d}t| \sim f^2, \tag{10}$$

which is close to the universal power law [see Equation (1)]. The close relationship between $\mathrm{d}f/\mathrm{d}t$ and f can be interpreted as the property of the shock propagation in the corona and

IP medium. In spite of this overall agreement, there is considerable deviation from $\epsilon \sim 2$ when individual frequency domains are considered. Aguilar-Rodriguez *et al.* (2005) noted that ϵ can be as high as 2.3 in the kilometric domain and as low as 1.4 in the metric domain. In the following, we shall demonstrate that this variation can be explained in terms of the different variations of the shock speed and the plasma density in different spatial domains between the Sun and Earth.

Gopalswamy (2006b) pointed out that the assumption of constant V may be reasonable in individual wavelength domains (metric, DH, or kilometric), but it may not be valid over the entire wavelength range. For example, CMEs associated with DH type II bursts are known to undergo rapid deceleration within the SOHO/LASCO field of view (Gopalswamy *et al.*, 2001b). We also know that CMEs and shocks undergo significant change in speed between the Sun and 1 AU (Gopalswamy *et al.*, 2000) because of the drag force of the ambient medium acting on the CMEs (Gopalswamy *et al.*, 2001b; Vršnak, 2001). Vršnak *et al.* (2001) had considered the decline of the shock speed in the near-Earth IP medium (kilometric domain). Here we generalize the speed variation in all the spatial domains by introducing a radial dependence for V of the form

$$V \sim r^{\beta}, \tag{11}$$

into Equation (9). This means $\beta > 0$ for the metric domain and $\beta < 0$ for the kilometric domain to explain the deviations from $\epsilon \sim 2$. Substituting Equation (11) for V into Equation (9) and making use of Equation (3) we get

$$|\mathrm{d}f/\mathrm{d}t| \sim f^{(\alpha+2\beta+2)/\alpha}. \tag{12}$$

Comparing (12) and (1) we see that

$$\epsilon = (\alpha + 2\beta + 2)/\alpha. \tag{13}$$

In the following we investigate Equation (8) using the observational results presented in this paper.

4.1. Metric Domain

Making use of the dynamic spectra of the 10 metric type II bursts available online (NGDC), we measured the drift rate of the fundamental components, where available. Figure 15 shows a scatter plot between $\mathrm{d}f/\mathrm{d}t$ and f for the 10 bursts. The scatter plot represents a power law of the form $|\mathrm{d}f/\mathrm{d}t| \sim f^{1.07}$ for the 10 events and $|\mathrm{d}f/\mathrm{d}t| \sim f^{1.27}$ when the 10 events were combined with the 58 metric type II bursts published by Mann *et al.* (1996). Out of the 65 events published by Mann *et al.* (1996), we chose only those events for which the drift rates of the fundamental components were measured. This value of ϵ is slightly smaller than the value 1.44 obtained by Aguilar-Rodriguez *et al.* (2005). In another study of 18 bursts that had clear band-splitting, Vršnak *et al.* (2002) obtained $\epsilon \sim 1.89$, similar to the universal value, but they had data to frequencies as low as 18 MHz.

As the observations presented in the preceding sections show, the CME speed (as well as the shock speed) increases during the metric type II burst. The assumption we make here is that the radial dependence of the shock mimics that of the CMEs. This is not a bad assumption so long as the shock is driven by the CME (see, *e.g.*, Gopalswamy *et al.*, 2005). Therefore, we expect $\beta > 0$ in Equation (11). If we assume that the heliocentric distance of the shock is not too different from that of the CME (as supported by the height – time plots),

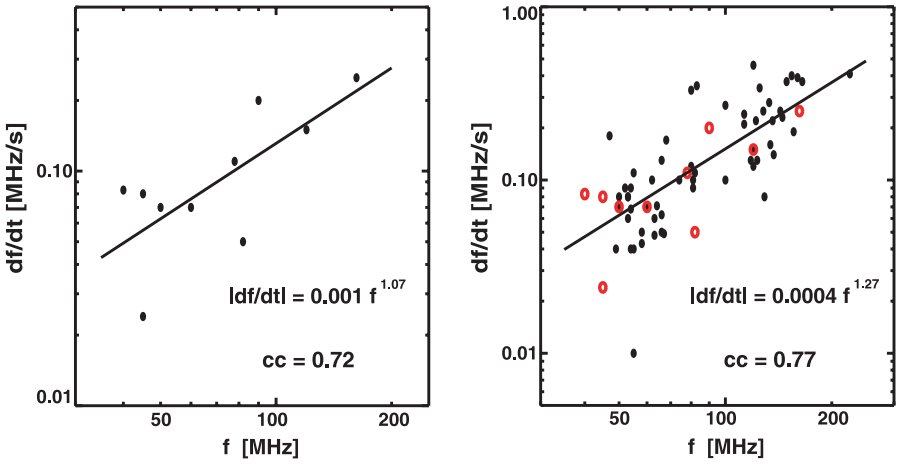

Figure 15 Scatter plot between the starting frequency f and the drift rate $\mathrm{d}f/\mathrm{d}t$ (absolute value) for the 10 metric type II bursts (left) and a similar plot from Potsdam data reported in Mann *et al.* (1996) with the data points from the left superposed. The scatter plots represent a power law of the form $|\mathrm{d}f/\mathrm{d}t| \sim f^{\epsilon}$ with $\epsilon = 1.07$ for the 10 events and 1.27 for the 10 events combined with the 58 events from Mann *et al.* (1996).

we can take the CME speed to be roughly the same as the shock speed for the duration of the type II bursts. We also need the space speed of the CME to get the spatial dependence of V [i.e., to obtain β in Equation (11)]. For this purpose, we choose only those events that are limb events from the view of at least one of the spacecraft (SA, SB, or SOHO). From Table 2, we see that the February and May 2007 events are all disk events for both the STEREO spacecraft (since the separation is not large enough). Similarly, the August 2007 event and the April 2008 event are disk events for all the spacecraft (including SOHO). This leaves only four limb events: 25 January, 3 June, and 31 December events in 2007 and the 25 March event in 2008. For the 25 January 2007 event, the CME first appeared in the COR1 FOV at 06:53:25 UT at $r = 2.85 R_{\mathrm{s}}$. The metric type II burst had already ended by this time, so it was not possible to detect the initial acceleration of the CME. Only for the 31 December 2007 and 25 March 2008 CMEs did we have adequate COR1 height – time measurements to derive the variation of V as a function of r. Of these, the 31 December 2007 event had the largest number of data points, so we can characterize the speed variation with height accurately.

Figure 16 shows how V varies with r for the 31 December 2007 and 25 March 2008 events. For the December event, COR1 captured the CME in four frames (both SA and SB). The CME manifestation was also observed in EUVI (two frames in SA and one frame in SB). The combined data show that the CME starts with a low speed of $\sim 450\ \mathrm{km\,s^{-1}}$, reaches a peak speed of $\sim 1000\ \mathrm{km\,s^{-1}}$, and then declines to $\sim 700\ \mathrm{km\,s^{-1}}$ in the outer corona. By plotting V as a function of r, we find that $V \sim r^{0.79}$ for both SA and SB, so $\beta = -0.79$. We now need α in the metric wavelength domain to obtain ϵ. Although $\alpha \sim 2$ is applicable to the IP medium, it is well known that the coronal density (where metric type II bursts occur) drops off steeply with distance, giving $\alpha \sim 6$ (see Saito, 1970; Leblanc *et al.*, 1998; or data in Newkirk, 1967). Substituting $\alpha = 6$ and $\beta = -0.79$ in Equation (13) we get $\epsilon = 1.04$. This is in close agreement with $\epsilon = 1.07$ obtained in Figure 15 and not too different from 1.27 obtained for all metric type II bursts.

The number of data points in the V versus r plot is small for the 25 March 2008 event. Nevertheless, we were able to obtain the power-law indices from SA and SB data:

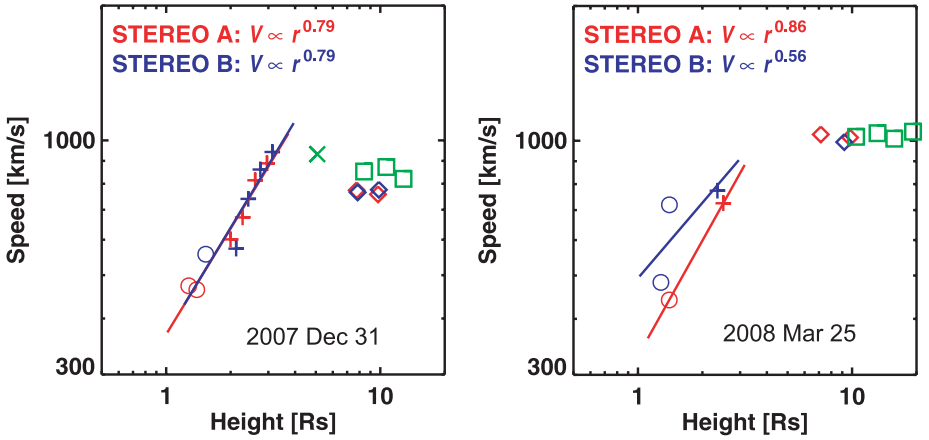

Figure 16 The variation of CME speed with height for the 31 December 2007 (left) and 25 March 2008 (right) events. Measurements from different instruments are distinguished: circles, EUVI; plus symbols, COR1; cross symbol, LASCO/C2; diamonds, COR2; squares, LASCO/C3. The speeds were obtained using four successive height – time data points at each height.

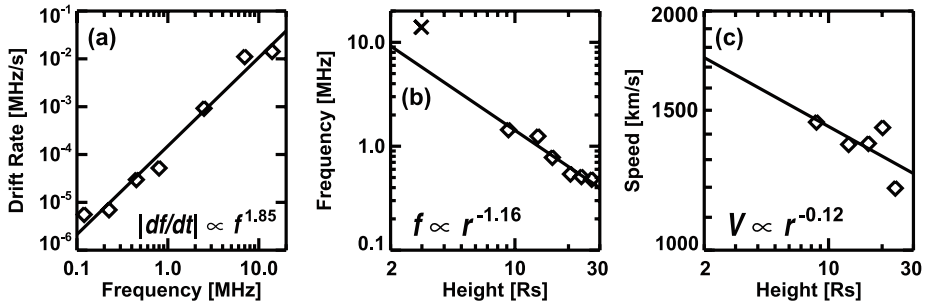

Figure 17 The drift-rate spectrum (a), the frequency variation with heliocentric distance (b), and the radial variation of CME speed (c) for the 25 January 2007 type II burst, the only event with emission components in the kilometric domain. In (b), the cross represents the 14-MHz data point not included in the fit because it is at the transition between metric and kilometric domains.

$\beta = -0.86$ for SA and $\beta = -0.56$ for SB. Recalling the discussion in Section 3.2 that the 25 March 2008 eruption is a good limb event only in SA view, we can take the SA data to be free of projection effects. Therefore, $\beta = -0.86$ and $\alpha = 6$ in Equation (13) give $\epsilon = 1.05$, which is similar to the value obtained from the 31 December 2007 event. Thus we conclude that the CME speed variation captured by COR1 correctly explains the behavior of the drift-rate spectrum in the metric domain. A further implication of this result is the close physical connection between type II radio bursts and CMEs.

4.2. Kilometric Domain

Out of the six type II bursts observed in the DH domain, only one extended to kilometric wavelengths (down to 90 kHz). The type II burst was observed both by WAVES and S/WAVES. For a single event like this, we can obtain the drift-rate spectrum by measuring the drift rate at many segments of the dynamic spectrum as we did in Section 3.4. Fig-

ure 17a shows the drift-rate spectrum, which has a power-law index of 1.85. This is significantly larger than the index (1.27) for the metric type II bursts and only slightly larger than the index (1.80) for all wavelength domains. Let us see how we can obtain $\epsilon = 1.85$ from Equation (13). Since we have CME observations overlapping with the spatial domain of the metric – kilometric type II burst, we can directly obtain the radial dependence of the emission frequency and compare it with the relation $f(r) \sim r^{-\alpha/2}$ [Equation (3)] to get α. For the set of times at which the CME heights were measured, we obtained the corresponding emission frequencies from the WAVES dynamic spectrum giving a set of frequency – height data points as plotted in Figure 17b. The scatter plot can be fit with a straight line, which gives the power-law index as 1.16, which is $\alpha/2$ according to Equation (3). The resulting $\alpha = 2.32$ is slightly higher than the canonical value of 2 (see, *e.g.*, Leblanc *et al.*, 1998; Reiner *et al.*, 1998; Pohjolainen *et al.*, 2007). The CME observations can also be used to obtain β by estimating the radial dependence of CME speed as we did for the metric emission range. Recall from Section 3.4 that the frequency of emission was ~ 500 kHz when the CME reached the edge of the LASCO/C3 FOV, overlapping with the spatial domain corresponding to the kilometric wavelengths. We computed the radial dependence of V using three height – time data points at a time. Figure 17c shows that V declines with r characterized by a power-law index $\beta = 0.12$. Note that β is now positive, opposite to what we found in the inner corona (see Figure 16). Using $\alpha = 2.32$ and $\beta = 0.12$ in Equation (13), we get $\epsilon = 1.97$, in good agreement with the value (1.85) obtained from the radio dynamic spectrum. If we use the canonical value of $\alpha = 2$, we get $\epsilon = 2.12$. Vršnak *et al.* (2001) used shock speed as a function of heliocentric distance inferred from density models and obtained $\beta = 0.13$, which is consistent with the value (0.12) obtained here using CME observations. As noted before, we have tacitly assumed that the shock speed is the same as the CME speed. We thus conclude that the drift-rate spectrum at kilometric wavelengths is steeper than that in the metric wavelengths because of the opposite behavior of speed as a function of heliocentric distance.

5. Discussion and Summary

The inner coronagraph COR1 onboard STEREO has a field of view covering $1.4R_s$ to $4R_s$, which enables observing CMEs close to the onset of type II bursts. EUV waves were found in most of the cases well before the start of the type II bursts, indicating that the fast-mode wave around the CME becomes a shock when the CME becomes super-Alfvénic. In all the EUVI snapshots obtained during the metric type II bursts the EUV disturbance was found to match with the outermost edge of the white-light disturbance, suggesting that the CME is the driver of the EUV wave, which becomes a shock to produce the type II burst.

We were able to determine the speed evolution of CMEs in the inner corona, and the speed profile has some similarity to the Alfvén speed profile at least for the two well-observed events (31 December 2007 and 25 March 2008). It is fairly clear that the type II burst starts at a height where the Alfvén speed is minimum in the corona (see Figure 5). But the height at which the type II burst ends depends on the relative variation of the CME speed and the coronal Alfvén speed. In the three cases discussed extensively, the type II burst ends when the CME reaches a heliocentric distance where the Alfvén speed peaks. The type II burst seems to end when the shock becomes subcritical or dissipates as an MHD wave in the high- Alfvén speed region. In two events, the speed had an impulsive behavior, very similar to that of the soft X-ray profiles. The radio emission ended even before the height at which the Alfvén speed reached its peak value. Zhang *et al.* (2001) reported a CME

associated with the impulsive flare of 16 May 1997 at 12:54 UT (duration $\sim$ 15 minutes). However, Zhang *et al.* (2001) did not find the CME speed behavior to follow the X-ray spike. A detailed examination of soft X-ray images from *Yohkoh* revealed a post-eruption arcade, and the flare actually was of long duration with the impulsive spike superposed on it. The long-duration flare started around 12:10 UT on 16 May 1997 and continued beyond 16 UT. Zhang *et al.*'s CME speed profile followed this long-duration flare rather than the impulsive spike. In contrast, the CME speed profile in our case followed the impulsive spike.

For the three events in which we were able to measure the CME height at the time of the metric type II burst onset, we found that the CME leading edge was at heights of $\sim 1.39 R_s$, $1.5 R_s$, and $1.66 R_s$ (for an average of $1.55 R_s$). This average value is remarkably similar to the height at which the coronal Alfvén speed attains a minimum value ($\sim 1.4 R_s$; see Figure 5) between the active region and the quiet coronal values (Gopalswamy *et al.*, 2001a; Mann *et al.*, 2003). This is significantly lower than the corresponding CME height ($2.2 R_s$) obtained from LASCO data alone. One can think of two reasons for this difference: *i*) The LASCO observations do not capture the initial speed variation of the CME and thus correspond to higher average speeds; *ii*) the plasma level in the corona for a given frequency may shift to larger or smaller heliocentric distances, depending on the phase of the solar cycle. It has been reported that the coronal density during the solar maximum is higher by a factor of four than that in the declining phase (MacQueen *et al.*, 2001). Since the type II bursts in this paper correspond to the declining phase of solar cycle 23, we expect that a given plasma level would move closer to the Sun compared to the solar maximum phase. Cliver *et al.* (2004) reported a metric type II burst on 6 November 1997 with CME observation available (from LASCO/C1) close to the onset of the burst; they estimated the CME height to be $\sim 1.33 R_s$ at metric type II onset. Since this event occurred during the minimum phase it is consistent with our conclusion that the low CME height at type II start may be due to the solar cycle effect. The density variation over the solar cycle may also have an influence on the radial profile of the Alfvén speed, but this needs a careful consideration including incorporation of the magnetic field variation in the corona.

We also set out to understand the deviations from the power-law nature of the drift-rate spectrum of type II radio bursts. The deviations are the decrease in the power-law index at metric wavelengths and the increase in the kilometric wavelength domain with respect to the overall value of 2 corresponding to the entire wavelength domain (metric to kilometric wavelengths). We provided observational evidence to show that these deviations are a direct consequence of the CME speed increase in the inner corona and decrease in the IP medium. Whereas the speed decrease in the IP medium was quantified from shock speeds inferred from density models (Vršnak *et al.*, 2001), we have obtained the speed variation from CME data. In addition, we found that the speed variation in the inner corona is opposite to that from the IP medium and can be directly linked to the positive acceleration of CMEs.

In summary, we were able to show that MHD fast-mode shocks form very low in the corona, when the CME leading edge is only $\sim 1.5 R_s$ from the Sun center using data from the inner coronagraph (COR1) onboard the STEREO mission. This distance also coincides with the spatial domain where the coronal Alfvén speed attains a minimum value. How the shock survives beyond this point depends on the relative increase in CME speed and the Alfvén speed. The CME speed and the Alfvén speed seem to reach their peak values around the $3 R_s - 4 R_s$ in the corona, and many type II bursts end around this time because the associated shocks become subcritical or dissipate. When the CME speed is much higher than the peak Alfvén speed, then it can drive the shock far into the IP medium resulting in the interplanetary type II burst, as was the case for the 25 January 2007 event. It is possible that the CME height at the time of the type II burst onset depends on the phase of the solar cycle,

but this needs further investigation. While the speed in the inner corona increases owing to the propelling force, the CME speed decreases in the IP medium from the drag force. This opposite tendency in CME speed variation can be quantified as a power law with positive (inner corona) and negative (IP medium) indices that naturally explain the deviations of the universal drift-rate spectrum of type II bursts. Such an explanation is consistent with the CME driving the shock irrespective of the spectral domain in which type II bursts are observed.

Acknowledgements The SECCHI instrument was constructed by a consortium of international institutions: the Naval Research Laboratory (USA), the Lockheed Martin Solar and Astrophysical Laboratory (USA), the NASA Goddard Space Flight Center (USA), the Max Planck Institut für Sonnensystemforschung (Germany), the Centre Spatial de Liège (Belgium), the University of Birmingham (UK), the Rutherford Appleton Laboratory (UK), the Institut d'Optique (France), and the Institute d'Astrophysique Spatiale (France). The S/WAVES instrument was built by a consortium including Observatoire de Paris (France), University of California at Berkeley (USA), University of Minnesota (USA), NASA Goddard Space Flight Center (USA), and AAS Space Research Institute (Austria). SOHO is a project of international collaboration between ESA and NASA. We thank the anonymous referee for helpful comments.

References

Aguilar-Rodriguez, E., Gopalswamy, N., MacDowall, R.J., Yashiro, S., Kaiser, M.L.: 2005, In: *Proceedings of Solar Wind 11/SOHO 16*, 393.

Bougeret, J.-L., Kaiser, M.L., Kellogg, P.J., Manning, R., Goetz, K., Monson, S.J., Monge, N., *et al.*: 1995, *Space Sci. Rev.* **71**, 231.

Bougeret, J.L., Goetz, K., Kaiser, M.L., Bale, S.D., Kellogg, P.J., Maksimovic, M., Monge, N., *et al.*: 2008, *Space Sci. Rev.* **136**, 487.

Brueckner, G.E., Howard, R.A., Koomen, M.J., Korendyke, C.M., Michels, D.J., Moses, J.D., Socker, D.G., *et al.*: 1995, *Solar Phys.* **162**, 357.

Cliver, E.W., Nitta, N.V., Thompson, B.J., Zhang, J.: 2004, *Solar Phys.* **225**, 105.

Gopalswamy, N.: 2006a, *J. Astrophys. Astron.* **27**, 243.

Gopalswamy, N.: 2006b, In: Gopalswamy, N., Mewaldt, R., Torsti, J. (eds.) *Solar Eruptions and Energetic Particles*, *Geophys. Monogr. Ser.* **165**, AGU, Washington, 207.

Gopalswamy, N., Kaiser, M.L.: 2002, *Adv. Space Res.* **29**(3), 307.

Gopalswamy, N., Thompson, B.J.: 2000, *J. Atmos. Solar Terr. Phys.* **62**, 1457.

Gopalswamy, N., Lara, A., Lepping, R.P., Kaiser, M.L., Berdichevsky, D., St. Cyr, O.C.: 2000, *Geophys. Res. Lett.* **27**, 145.

Gopalswamy, N., Lara, A., Kaiser, M.L., Bougeret, J.-L.: 2001a, *J. Geophys. Res.* **106**, 25261.

Gopalswamy, N., Yashiro, S., Kaiser, M.L., Howard, R.A., Bougeret, J.-L.: 2001b, *J. Geophys. Res.* **106**, 29219.

Gopalswamy, N., Aguilar-Rodriguez, E., Yashiro, S., Nunes, S., Kaiser, M.L., Howard, R.A.: 2005, *J. Geophys. Res.* **110**, A12S07.

Gopalswamy, N., Yashiro, S., Xie, H., Akiyama, S., Aguilar-Rodriguez, E., Kaiser, M.L., Howard, R.A., Bougeret, J.-L.: 2008a, *Astrophys. J.* **674**, 560.

Gopalswamy, N., Yashiro, S., Akiyama, S., Mäkelä, P., Xie, H., Kaiser, M.L., Howard, R.A., Bougeret, J.-L.: 2008b, *AnnGeo* **26**, 3033.

Holman, G.D., Pesses, M.E.: 1983, *Astrophys. J.* **267**, 837.

Howard, R.A., Moses, J.D., Vourlidas, A., Newmark, J.S., Socker, D.G., Plunkett, S.P., Korendyke, C.M., *et al.*: 2008, *Space Sci. Rev.* **136**, 67.

Kaiser, M.L., Kucera, T.A., Davila, J.M., St. Cyr, O.C., Guhathakurta, M., Christian, E.: 2008, *Space Sci. Rev.* **136**, 5.

Leblanc, Y., Dulk, G.A., Bougeret, J.-L.: 1998, *Solar Phys.* **183**, 165.

Mann, G., Klassen, A., Classen, H.T., Aurass, H., Scholz, D., MacDowall, R.J., Stone, R.G.: 1996, *Astron. Astrophys.* **119**, 489.

Mann, G., Klassen, A., Estel, C., Thompson, B.J.: 1999, In: Vial, J.-C., Kaldeich-Schmann, B. (eds.) *Proc. of 8th SOHO Workshop*, 477.

Mann, G., Klassen, A., Aurass, H., Classen, H.-T.: 2003, *Astron. Astrophys.* **400**, 329.

MacQueen, R.M., Burkepile, J.T., Holzer, T.E., Stanger, A.L., Spence, K.E.: 2001, *Astrophys. J.* **549**, 1175.

Michalek, G., Gopalswamy, N., Xie, H.: 2007, *Solar Phys.* **246**, 409.
Newkirk, G.A.: 1967, *Ann. Rev. Astron. Astrophys.* **5**, 213.
Pohjolainen, S., van Driel-Gesztelyi, L., Culhane, J.L., Manoharan, P.K., Elliott, H.A.: 2007, *Solar Phys.* **244**, 167.
Reiner, M.J., Kaiser, M.L., Fainberg, J., Stone, R.G.: 1998, *J. Geophys. Res.* **103**, 29651.
Saito, K.: 1970, *Ann. Tokyo Astron. Obs. Ser. 2* **12**, 53.
Saito, K., Poland, A.I., Munro, R.H.: 1977, *Solar Phys.* **55**, 121.
Sheeley, N.R. Jr., Wang, Y.-M., Hawley, S.H., Brueckner, G.E., Dere, K.P., Howard, R.A., *et al.*: 1997, *Astrophys. J.* **484**, 472.
Thompson, B.J., Cliver, E.W., Nitta, N., Delannée, C., Delaboudinière, J.-P.: 2000, *Geophys. Res. Lett.* **27**, 1431.
Vršnak, B.: 2001, *Solar Phys.* **202**, 173.
Vršnak, B., Aurass, H., Magdalenic, J., Gopalswamy, N.: 2001, *Astron. Astrophys.* **377**, 321.
Vršnak, B., Magdalenić, J., Aurass, H., Mann, G.: 2002, *Astron. Astrophys.* **396**, 673.
Vršnak, B., Cliver, E.: 2008, *Solar Phys.* **253**, 215.
Wood, B.E., Karovska, M., Chen, J., Brueckner, G.E., Cook, J.W., Howard, R.A.: 1999, *Astrophys. J.* **512**, 484.
Zhang, J., Kundu, M.R., White, S.M., Dere, K.P., Newmark, J.S.: 2001, *Astrophys. J.* **561**, 396.